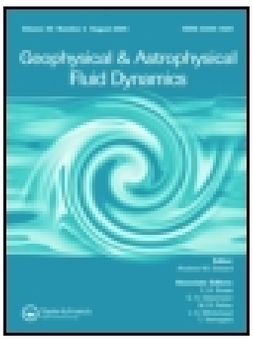

Geophysical & Astrophysical Fluid Dynamics

ISSN: 0309-1929 (Print) 1029-0419 (Online) Journal homepage: http://www.tandfonline.com/loi/ggaf20

Topographically generated steady currents in barotropic turbulence

A. M. Treguier

To cite this article: A. M. Treguier (1989) Topographically generated steady currents in barotropic turbulence, Geophysical & Astrophysical Fluid Dynamics, 47:1-4, 43-68, DOI: 10.1080/03091928908221816

To link to this article: http://dx.doi.org/10.1080/03091928908221816

Published online: 19 Aug 2006.

Geophys. Astrophys. Fluid Dynamics, Vol. 47, pp. 43–68
Reprints available directly from the publisher
Photocopying permitted by license only

TOPOGRAPHICALLY GENERATED STEADY CURRENTS IN BAROTROPIC TURBULENCE

A. M. TREGUIER

National Center for Atmospheric Research, PO Box 3000, Boulder, CO 80307, USA

(*Received 1 September 1988; in final form 11 November 1988*)

Steady currents develop in oceanic turbulence above topography even in the absence of steady forcing. Mesoscale steady currents are correlated with mesoscale topography with anticyclonic eddies above topographic bumps, and large scale westward flows develop when β is non-zero. The relationship between those two kinds of steady currents, as well as their dependence on various parameters, is studied using a barotropic quasi-geostrophic channel model. The percentage of steady energy is found to depend on the forcing, friction and topography in a non-monotonic fashion. For example, the percentage of steady currents grows with the energy level in the linear regime (low energies) and decreases when the energy level increases in the nonlinear regime (high energies). Mesoscale steady currents are the energy source for the steady westward flow $\bar{U}$, and therefore $\bar{U}$ is the maximum when large scale and mesoscale currents are of the same order of magnitude. This happens when the ratio S of the large scale slope $\beta H/f_0$ and the mesoscale rms topographic slope α is of order one. $\bar{U}$ decreases for both small and large values of S.

KEY WORDS: Ocean turbulence, topographic eddies.

1. INTRODUCTION

One important effect of bottom roughness on an overlying turbulent flow is to generate steady currents, even in the absence of a steady forcing. In the existing studies, steady currents are traditionally divided into "mesoscale" and "large scale" currents.

Mesoscale steady currents have horizontal scales similar to the typical size of oceanic eddies, roughly 100 km, and are generated by mesoscale topographic features. Their emergence in quasi-geostrophic turbulence above topography has been demonstrated by the free decaying turbulence experiments of Bretherton and Haidvogel (1976). In those simulations, the flow evolves toward a quasi-steady pattern characterized by anticyclonic eddies above the topographic elevations (and cyclonic above depressions). Similar steady currents appear even when the flow remains strongly fluctuating, as in the statistical equilibrium solution of Salmon *et al.* (1976), or the forced barotropic model of Herring (1977).

Large scale steady currents are defined as following "large scale" ($\geqq 1000$ km) potential vorticity gradients. The distinction between "mesoscale" and "large scale" currents arises naturally when the former are generated by mesoscale topography, and the latter by the large scale potential vorticity gradient due to the β-effect. When large scale currents are associated with large scale topographic features, the distinction becomes arbitrary since bottom topography has a broad band spec-

trum. However, it is still possible (and useful) to distinguish the two kinds of currents in numerical models with idealized topographies. For example, Haidvogel and Brink (1986) used a large scale topography representing the continental slope with mesoscale variations on it, and showed that a steady alongslope large scale current is generated when there is no steady forcing.

Early studies showed how pre-existing large scale currents are affected by the topography. The simulations of Bretherton and Karweit (1975) demonstrated that an eastward flow is effectively slowed down by the topography, whereas a westward flow is not. The topographic drag is not symmetric on a β plane because an eastward flowing current generates a standing Rossby wave above a topographic feature and therefore loses energy whereas a westward flowing current does not. This asymmetry intuitively helps one to understand why a steady westward flow is generated when the forcing has a zero time mean. However, in numerical simulations of such flows (like the ones to be presented here), the topographic term in the large scale momentum balance does not behave like an asymmetric drag. It is not a sink of eastward momentum at all times and is not always larger when the large scale flow is eastward. A better explanation of the westward flow generation in β-plane topographic turbulence is given by Holloway (1987). Three processes are involved:

1) Nonlinear eddy interactions generate a "mesoscale" steady flow correlated with the topography, as mentioned above.
2) The β effect tends to induce a westward phase of this steady mesoscale flow.
3) Since positive pressure anomalies (positive P) tend to lie westward of topographic elevations, the spatially averaged topographic drag $\langle -P\,\partial h/\partial x\rangle$ is negative, and tends to generate westward momentum.

Holloway's explanation shows that the two kinds of steady currents are linked, the presence of a steady mesoscale flow being necessary for the existence of the large scale westward currents. However, most previous studies have ignored that fact and focused on one or the other category. The first aim of the numerical simulations presented here is to show the relationship betwen the two kinds of steady currents by using energy budgets, and to determine their relative importance in terms of energy content. The other aim of our study is a more complete exploration of the parameter space. Analysis of weakly nonlinear flow over topography (Samelson and Allen, 1987) on one hand, and statistical turbulence models (Herring, 1977; Holloway, 1978) on the other hand suggest a different dependence of steady currents on the parameters. Our simulations confirm the existence of a quasi-linear and a nonlinear regime, which result in a non-monotonic dependence of the percentage of steady currents on the forcing, friction, or topography.

In order to achieve this extensive exploration of the parameter space, we have focused on a simple problem, and considered only barotropic flows. Steady currents generated by the topography are certainly bottom-intensified, and the present study is only a first step towards understanding the more complicated baroclinic case.

In the following section, steady solutions valid in unforced flows are reviewed, and the energy equations show how those solutions may be modified when forcing and friction are present. The behavior suggested by this analysis is then demonstrated by numerical experiments on an f-plane (Section 4) and on a β-plane (Section 5), following a brief description of the model and strategy (Section 3). The results are summarized in Section 6.

2. STEADY SOLUTIONS AND THEIR DYNAMICS

2.1 Equations

Barotropic quasi-geostrophic flow in a zonal β-plane channel is described by a streamfunction

$$\Psi(x, y, t) = \psi(x, y, t) - U(t)y, \tag{1}$$

where ψ is zero on the north and south boundaries, and periodic in the east–west direction. The prediction equation for ψ is the quasi-geostrophic vorticity equation

$$\frac{\partial \zeta}{\partial t} + \beta \frac{\partial \psi}{\partial x} + J(\psi, \zeta + \tilde{h}) + U \frac{\partial (\zeta + \tilde{h})}{\partial x} = \frac{(\nabla \times \tau)_z}{\rho H} - \varepsilon \zeta - \nu \nabla^6 \psi, \tag{2}$$

where $\zeta = \nabla^2 \psi$ is the relative vorticity, τ the wind stress, ε^{-1} the bottom friction decay time, ν the coefficient of biharmonic friction, and $\tilde{h} = f_0 h/H$ with H the total ocean depth, $h(x, y)$ the bottom topography and f_0 the Coriolis frequency. The meridional velocity vanishes on the north and south walls of the channel:

$$\frac{\partial \psi}{\partial x} = 0, \quad \text{for } y = y_N \text{ and } y = y_S, \tag{3}$$

and additional boundary conditions are needed because of the biharmonic friction operator

$$\nabla^2 \psi = 0, \nabla^4 \psi = 0, \quad \text{for } y = y_N \text{ and } y = y_S. \tag{4}$$

The prediction equation for U must be derived from momentum or energy conservation (McWilliams, 1977). The zonal momentum equation integrated over the channel shows the relation between U and the topography

$$\frac{\partial U}{\partial t} = T + A^{-1} \int\int \frac{\tau_x}{\rho H} dx\, dy - \varepsilon U, \tag{5}$$

where A is the total area, and $T = A^{-1} \int\int v\tilde{h}\, dx\, dy$ is the topographic drag.

2.2 Simple Steady Solutions

Let us first review the steady solutions of (2) and (5) when there is no forcing or friction. The steady components will be noted by an overbar, representing a time-average. $\bar{\psi}$ satisfies $J(\bar{\psi}-\bar{U}y, \bar{\zeta}+\tilde{h}+\beta y)=0$ and therefore $\bar{\psi}-\bar{U}y=\mathscr{F}(\bar{\zeta}+\tilde{h}+\beta y)$, $\mathscr{F}$ being an arbitrary function. The simplest solution is for a linear $\mathscr{F}$

$$\bar{\psi}=\kappa^{-2}(\bar{\zeta}+\tilde{h}), \qquad \bar{U}=-\beta\kappa^{-2}, \tag{6}$$

κ^{-2} being a constant. In the inviscid case κ^2 may be negative, but only when the finite resolution of the model allows enstrophy to concentrate at the smallest scale, and therefore all "physical" solutions correspond to a positive κ^2 (Carnevale and Frederiksen, 1987). When β is zero, a solution is possible without a large scale current $\bar{U}$. The characteristics of the solution are shown better by its Fourier transform in wavenumber space $\overline{\psi}^*(K)$,

$$\overline{\psi}^*(K)=\frac{\tilde{h}^*(K)}{K^2+\kappa^2}. \tag{7}$$

$\bar{\psi}$ is therefore a low-pass filtered version of the topographic field. At large scales ($K \ll \kappa$), $\bar{\psi}$ is proportional to the topography. At small scales ($K \gg \kappa$), the vorticity is proportional to $-\tilde{h}$, and the vorticity and the topography are anticorrelated.

Note that the topographic drag vanishes for this inviscid solution, even on a β-plane. A topographic drag must exist during the initial adjustment, but at equilibrium advection by U cancels the tendency for westward propagation induced by β and the topographic drag is zero. It may seem paradoxical that $\bar{U}$ is independent of $\tilde{h}$ in (6), and does not vanish in the limit $\tilde{h}\to 0$. In that limit no topographic drag can exist even during the initial adjustment. Therefore U is no longer coupled with the mesoscale flow and is just an arbitrary invariant (Carnevale and Frederiksen, 1987).

Besides being the simplest solution, (6) is the most likely solution in at least two cases. The first case is statistical equilibrium flows, e.g., flows with a finite number of degrees of freedom and totally free of forcing and dissipation. Such flows happen only in truncated numerical models and not in physical fluids, but are nevertheless interesting because the flow tends towards a maximum entropy solution (provided the ergodic hypothesis is satisfied) which can be calculated analytically and depends only on the time invariants (total energy, total enstrophy and topography). Salmon *et al.* (1976) and more recently Carnevale and Frederiksen (1987) have shown that statistical equilibrium flows above topography are not completely steady in most cases, but they have a steady component satisfying (6).

The second case in which (6) appears as a possible solution is freely decaying turbulence. When only high order friction is present, energy decays very slowly but relative enstrophy is strongly dissipated. Bretherton and Haidvogel (1976) have suggested that *potential* enstrophy also decreases and that the flow tends towards

the solution (6) because is has the minimum potential enstrophy for a given energy. However, potential enstrophy decreases only if the vorticity ζ is larger than the topography $\tilde{h}$ for the small spatial scales. The numerical simulations confirm that steady currents qualitatively similar to (6) develop, but the theoretical solution is not achieved exactly, and a large dissipation is needed for the flow to be completely steady.

2.3 Steady Currents Dynamics in a Forced Flow

2.3.1 f-plane case

In a flow with forcing and dissipation, a forcing term must be present to maintain steady currents against dissipation. The steady energy equation is obtained by multiplying (2) by $\bar{\psi}$, integrating over the domain and averaging in time

$$\int\int \overline{J(\psi', \zeta')}\bar{\psi} = -\int\int \nu(\nabla\bar{\psi})^6 - \int\int \varepsilon(\nabla\bar{\psi})^2. \tag{8}$$

The fluctuating quantities are noted by primes, the time average by an overbar, and the time average of the forcing is assumed to be zero. Equation (8) shows that steady currents are generated by *nonlinear interactions* only. The topographic term $J(\bar{\psi}', \tilde{h})\bar{\psi}$ vanishes when integrated over the domain, and no contribution arises from $J(\psi', \tilde{h})\bar{\psi}$ because the time average of that term is zero. The nonlinear term $J(\psi, \zeta)$ allows the generation of a zero frequency component $\bar{\psi}$ by the interaction of two components ψ and ζ having frequencies ω and $-\omega$, respectively. On the other hand, the topographic term $J(\psi, \tilde{h})$ cannot transfer energy between frequencies since the topography $\tilde{h}$ is constant in time.

A consequence is that no steady currents can exist in a linear solution without steady forcing. In a weakly nonlinear flow, a rough scaling of (8), neglecting biharmonic friction and assuming that the spatial scales associated with ψ' and $\bar{\psi}$ are similar, suggests that the importance of the steady currents should grow as the eddy enstrophy grows and as the friction decreases:

$$\frac{\bar{\psi}}{\psi'} \approx \frac{\zeta'}{\varepsilon}.$$

This scaling is in agreement with the solution of Samelson and Allen (1987). Those authors calculated steady currents for flow over topography on a β-plane with weak forcing, friction and nonlinearity, and a weak dependence on the y coordinate. In their analytical solution, $\bar{\psi}/\psi'$ varies like $\hat{\tau}/\hat{\varepsilon}$ the ratio of the nondimensional forcing and the nondimensional bottom friction.

In a fully nonlinear regime, on the other hand, steady currents are expected to decrease when the relative vorticity ζ' becomes large compared to the topography $\tilde{h}$. In that limit, the flow behaves like flat-bottom turbulence and, if the effects of boundaries are small enough so that the flow is isotropic and spatially homogeneous, no large rectified currents can develop. The percentage of steady currents

should be a decreasing function of the rms vorticity ζ' in the nonlinear regime (Herring, 1977).

The consideration of the quasi-linear and the nonlinear limits suggests that the percentage of steady currents does not depend monotonically on the energy level. Similarly, a complex dependence on the topography may be expected. The nonlinear forcing term $\overline{J(\psi', \zeta')}\bar{\psi}$ depends on h indirectly because h modifies the correlations between ψ', ζ' and $\bar{\psi}$. When h increases from zero for a given energy level, the percentage of steady currents first grows, but it may decrease when h is large enough so that the flow is quasi-linear. The simulations presented in the following sections confirm this behavior.

2.3.2 β-plane case

In the β-plane case, it is useful to write separate energy equations for mesoscale and large scale currents. The equation for the mesoscale $\bar{\psi}$ is simply (8) with an additional energy transfer $-\bar{U}\bar{T}$ on the right hand side. This term is proportional to the steady topographic drag $\bar{T} = A^{-1} \int\int \bar{v}\tilde{h}\, dx\, dy$ (A being the domain area). The energy equation for the westward flow $\bar{U}$,

$$\bar{U}\bar{T} = \varepsilon \bar{U}^2, \tag{9}$$

shows the coupling between the mesoscale steady flow $\bar{\psi}$ and the large scale steady flow $\bar{U}$. In the absence of steady forcing, the topographic drag term $\bar{U}\bar{T}$ is the only possible energy source. In our simulations, the westward steady flow $\bar{U}$ can draw energy from the steady mesoscale flow $\bar{\psi}$ because $\bar{T}$ is negative. For a forced steady eastward flow (as in Bretherton and Karweit, 1975), the topographic drag $\bar{T}$ is also negative, and therefore the large scale flow loses energy.

Scaling (9) shows that the westward flow $\bar{U}$ depends on the rms velocity of the mesoscale steady currents $\bar{u}$, and on the correlation C between $\bar{v}$ and h:

$$\bar{U} \approx \frac{\tilde{h}}{\varepsilon} \bar{u} C. \tag{10}$$

Since $\bar{u}$ and C in turn depend on the energy level, the topography and β, the effect of the parameters on the westward flow cannot be deduced from a simple scaling, but will be inferred from the numerical simulations presented in Section 5.

3. MODEL AND STRATEGY

3.1 Numerical Model

A zonal channel domain has been chosen here in order to be able to model the large scale zonal flow U induced by the β effect, while retaining some of the simplicity and spatial homogeneity associated with periodic boundary conditions.

Table 1 Parameters of the experiment F4[a]

Geometry	Domain size	L	1280 km
	Grid size	dx	20 km
	Resolution	N	64 points
	Ocean depth	H	5000 m
Forcing	Type	Stress	
	Rms τ_x/ρ	τ_0	$7.5\,10^{-4}\,m^2\,s^{-2}$
	Time scale	T_c	20 days
Friction	Bottom friction	ε	$10^{-7}\,s^{-1}$
	Biharmonic friction	A	$1.5\,10^{10}\,m^4\,s^{-1}$
Topography	Rms height	h	100 m
		$\delta = h/H$	0.02
	Spectral shape	$B(K)$	K^{-2}
	Rms slope	α	$1.4\,10^{-3}$

[a]In all following tables, parameters are the same as here except when otherwise indicated. The wind forcing type is either "stress" for a uniform zonal stress, or "curl" for a large scale curl with white wavenumber spectrum betweeen wavelengths of 1280 and 430 km. In both cases the amplitude of the forcing is given by the rms zonal stress τ_0. The topographic spectral shape is designated by $B(K)=K^{-2}$, $B(K)=K^{-3}$ or $B(K)=(14)$ for spectrum (14) with a peak at wavelength 160 km.

In a doubly periodic domain, it is possible to add a linear trend (Uy) to the streamfunction and use the additional equation (5) to calculate it, as was done by Holloway (1987). However, this is possible only in the barotropic case (Bretherton and Karweit, 1975). In the baroclinic case, it is impossible to derive a consistent equation for the time change of the large scale shear $U(z)$. A channel model is therefore necessary for later comparison with baroclinic simulations.

We have used the model of McWilliams and Chow (1981), modified to include bottom topography. The model solves the barotropic vorticity equation in finite-difference form. The nonlinear advection terms are calculated using an Arakawa Jacobian. The equation for U used in the model is the integral of the momentum equation on the south boundary

$$\int_0^{L_x} dx \left[\left(\frac{\partial}{\partial t} + \varepsilon + \nu \nabla^4 \right) \frac{\partial \psi}{\partial y} - \left(\frac{\partial}{\partial t} + \varepsilon \right) U + \frac{\tau_x}{\rho H} \right]_{y=0} = 0. \tag{11}$$

This equation is equivalent to (5) (McWilliams, 1977) and the finite difference form of (5) is satisfied in the model. The equations are integrated in time using a leap-frog scheme with an occasional predictor–corrector scheme to avoid time splitting of the solution. Friction terms are lagged in time.

3.2 Parameters

Table 1 gives the summary of the parameter values for a typical experiment, F4. Since a large number of simulations was necessary, a low resolution (64×64 grid

points) has been chosen. The size of the grid is 20 km, and the size of the square domain is 1280 km.

The forcing function is characterized by its time behavior and its spatial pattern. Two kinds of spatial patterns are used. The simplest one is a uniform zonal stress τ_x. This was the forcing used in Haidvogel and Brink's (1986) study of coastal currents. This forcing is special in the sense that there is no input of vorticity. In the absence of topography, the solution would be simply a uniform fluctuating zonal flow U. A more general forcing pattern consisting of a large scale wind stress curl is also used. The curl field is generated by assuming an isotropic white spectrum between wavelengths of 1280 and 430 km and a random phase, and performing a Fourier transform. The corresponding zonal wind stress, which is needed for the transport equation, is calculated from the curl by assuming that the wind stress field is non-divergent.

As for the time dependence, the simplest is a periodic function, as used by Haidvogel and Brink (1986). However, a periodic forcing makes the response very sensitive to small changes in parameters when the response has a resonant character. Another characteristic found in preliminary simulations with a periodic forcing is that a significant change in the steady current occurs when the energy level reaches a certain value, because the response evolves from a "periodic" behavior into a "chaotic" one (those terms refer to the qualitative appearance of the time series). This sharp transition between two regimes is associated with systems having few degrees of freedom, and it is not our purpose to study it. Therefore we prefer to eliminate it by using a non-periodic forcing. Note that Haidvogel and Brink obtained only the "periodic" type of response. Possibly, with a larger energy level or a topography with more degrees of freedom, they would also have observed a transition to a "chaotic" behavior.

Our choice for the time dependence of the forcing is a Markovian process as in Treguier and Hua (1987)

$$\frac{\partial \tau(x,y)}{\partial t} = -\omega_c \tau + G(x,y,t),$$

where $G(x,y,t)$ is a white noise process. A Markovian process with a time scale $T_c = 2\pi/\omega_c$ of a few days is quite representative of atmospheric variability. In fact, time scales smaller than 20 days tend to be filtered out since resonant barotropic Rossby waves with smaller periods cannot exist in our small (1280 km) domain. The only inconvenient aspect of the Markovian process is its non-zero time mean, which could generate steady currents even in the absence of any nonlinear rectification. This may be seen by considering its frequency spectrum

$$S_\tau(\omega) = \frac{|G^2|}{(\omega^2 + \omega_c^2)}, \tag{12}$$

G being a white noise process, $|G^2|$ is constant and the time average $S_\tau(0)$ is non zero. In order to ensure that the variance at zero frequency is small compared with

the total variance, one has to consider a series long enough compared with the characteristic time scale of the process. Our criterion for a "small" mean is that the input of steady energy from the wind in the energy budget must be at most 3% of the total input (eddy + steady energy). From the spectrum (12), a series of length $10T_c$ would seem sufficient. However, the oceanic response is a low-pass filter in time and in some cases we had to calculate diagnostics on time periods of $200T_c$ for our criterion to be satisfied.

The topographic field is randomly generated from a specified isotropic spectrum as in most previous studies in periodic models. The only difference is that we impose the boundary condition $\partial h/\partial x = 0$ at the north and south boundaries in order to avoid the formation of boundary layers. When $\partial h/\partial x$ is non-zero at the boundaries $J(\bar{\psi}, \tilde{h})$ is balanced by biharmonic friction, and a boundary layer forms with a width L_b depending on the biharmonic friction coefficient ν. Such a boundary layer was observed in test experiments and its width of order one grid point agreed with the value L_b derived from the vorticity balance at the boundary,

$$\nu \nabla^6 \bar{\psi} \approx \frac{\partial \bar{\psi}}{\partial y} \frac{\partial \tilde{h}}{\partial x} \quad \Rightarrow \quad L_b \approx \sqrt[5]{\frac{H\nu}{f_0 \alpha}}, \tag{13}$$

α being the rms topographic slope.

The model topography is characterized by its rms height h or the nondimensional height $\delta = h/H$ and its wavenumber spectrum $B(K)$ which may be either a K^{-2}, a K^{-3} spectrum, or a spectrum defined by

$$B(K) = \frac{AK}{3(K_p^4 + K^4)}. \tag{14}$$

This spectrum with a peak at wavenumber $K = K_p$ is less realistic but shows the influence of small scale topographies. The topographic scale can be represented by the wavenumber $\bar{K}_t$ defined as

$$K_t^2 = \frac{\int B(K) K^2 \, dK}{\int B(K) \, dK}. \tag{15}$$

The rms topographic slope α is defined by $\alpha = \bar{K}_t h$.

3.3 Statistical Significance of the Results

Most previous studies of flow over topography considered only one random realization of the topographic field, assuming that the flow was spatially homogeneous and ergodic, and that averaging in space and time was equivalent to an average over various realizations. However, one simulation (whatever its length) provides only *one* independent estimate of the *steady* currents. We thus performed various sets of simulations to get an idea of the statistical significance of this

estimate. Within each set of experiments, the parameters remained identical and only the random phase of the topography varied. We found that when the horizontal scale of the topography is large enough compared with the scale of the domain (mainly when a K^{-3} spectrum is used) the energy of the steady currents may vary by 20% to 50% from one simulation to the other, especially for the cases with low energy levels. On the other hand, when a K^{-2} spectrum is used, the steady currents vary at most by 5%. The strong dependence of the steady currents on the spatial pattern of the topography when the domain contains only a few large scale topographic features (case of the K^{-3} spectrum) is linked to the lack of spatial homogeneity in flow over topography noticed by Treguier and Hua (1988, Figure 12). In order to have a reliable estimate, one needs to average over a domain large enough compared with the typical topographic scale, or over different realizations. In most simulations presented here, the topography has a K^{-2} spectrum. A few simulations have been performed with a K^{-3} spectrum to show *qualitatively* the effect of an increase of the topographic scale. Since the quantitative results of such a simplified model are not of much interest, averaging was thought unnecessary.

The steady currents as well as the energy budgets have been calculated by averaging over the last 10 years of simulation. In simulations on an f-plane with a low energy level, 5 years were usually enough. On the other hand, for simulations with a high energy level or on a β-plane, there were still variations of about 10% between diagnostics based on 10 years and diagnostics based on 20 years. However, we do not consider 10% to be statistically significant and therefore we have run most simulations for 11 years (performing the diagnostics on the last 10 years).

4. SIMULATIONS IN AN f-PLANE CHANNEL

4.1 Dynamics

Steady currents are a very important component of the response in most of our experiments. In simulation F4 for example, a small topographic rms height (100 m) is sufficient to generate a large steady flow (representing about half of the total kinetic energy). This result however is model dependent. Barotropic models overestimate topographic effects because the bottom velocity is larger than that in stratified models in which the wind forcing acts only near the surface.

The time series of kinetic energy for experiment F4 (Figure 1) shows that long time scale variations are present in the response even though the characteristic time scale of the forcing is only of 20 days. The zonal transport variations are closer to the forcing time scale. In the absence of β, the time averaged transport is expected to be small, although non zero since the topographic drag does not vanish exactly, mainly because of dissipation. Here the time averaged transport is 55 Sv which is relatively small compared to the typical variations ($\approx$330 Sv).

Although there is no reason to expect either a maximum entropy solution of a minimal enstrophy solution to be achieved, steady currents in simulation F4 are

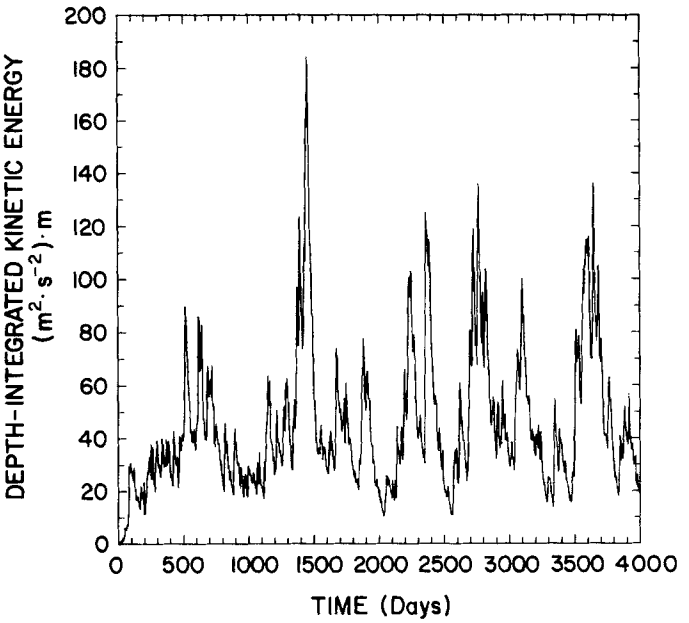

Figure 1 Time series of the depth-integrated kinetic energy (in $m^3 s^{-2}$) for experiment F4.

qualitatively similar to the simple inviscid solution (6). The correlation of the streamfunction and the topography at large scale, as well as the anticorrelation of the relative vorticity and the topography at small scale, appear clearly in the mean fields of Figure 2a. The linear relation (6) between $\bar{\psi}$ and $\bar{\zeta}+\tilde{h}$ is only approximately verified because of the forcing and dissipation as shown by the scatter plot in Figure 2b. As in Bretherton and Haidvogel's (1976) solution, different regions of the flow tend to have different values of the characteristic scale $2\pi/\kappa$, in the present case ranging roughly from 600 km to 900 km. Since $2\pi/\kappa$ is close to the size of the domain (1280 km), the anticorrelation between the vorticity $\bar{\zeta}$ and the topography is good (the coefficient is 0.9), while the correlation between the streamfunction ψ and the topography shows up only in scales larger than 600 km (the correlation coefficient is 0.3). A characteristic of the theoretical solution (6) pointed out by Herring (1977) is that at small scales $\bar{\zeta}\cdot\tilde{h}=-\tilde{h}^2$. This relation is approximately verified for this simulation for spatial scales smaller than 600 km as shown in Figure 3a, except at very small scales where biharmonic friction becomes important. The agreement is even better when the energy level is higher (Figure 3b) since the characteristic scale $2\pi/\kappa$ is larger than the domain size in that case. Such an agreement was also found in freely decaying turbulence experiments by Holloway (1978).

When the flow is forced by a large scale curl instead of a uniform wind stress, the percentage of steady energy tends to be lower (Table 2) and the departure from a single linear relationship between the streamfunction and potential vorticity is somewhat larger, especially at low energy levels. We have not tried to quantify the departure as a function of various parameters. Our main point here is that

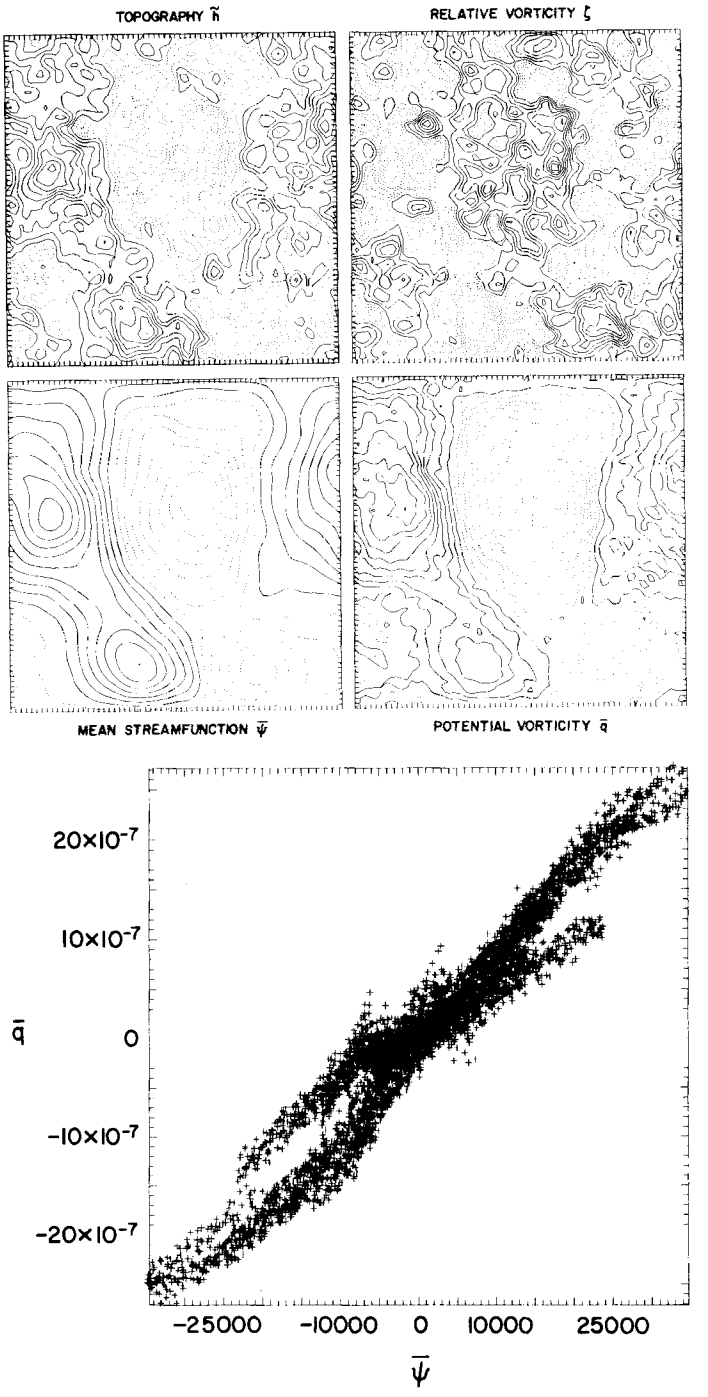

Figure 2 (a) Time-averaged fields for experiment F4. Contour intervals are 40 m for the topography, $5 \times 10^{-7}\,s^{-1}$ for the relative vorticity $\bar{\zeta}$, $4000\,m^2\,s^{-1}$ for the streamfunction $\bar{\psi}$, and $3 \times 10^{-7}\,s^{-1}$ for the potential vorticity $\bar{q} = \bar{\zeta} + \tilde{h}$; (b) Potential vorticity $\bar{q}$ as a function of $\bar{\psi}$ for all grid points in experiment F4.

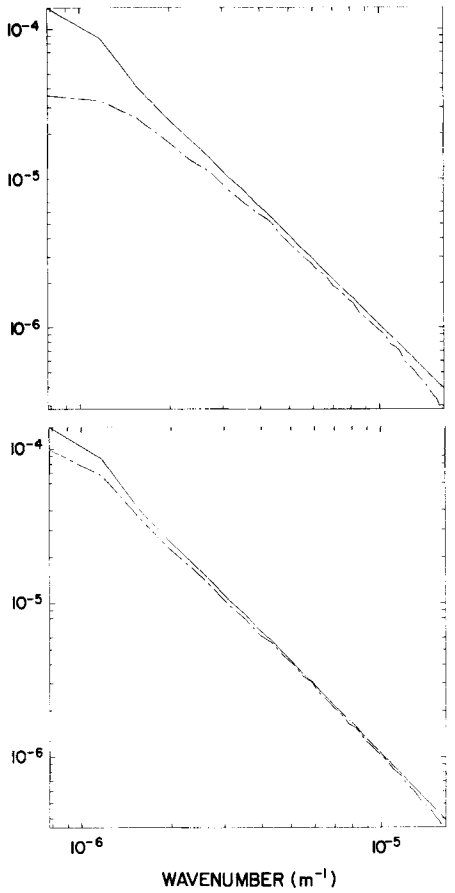

Figure 3 $-\tilde{\zeta}\tilde{h}$ (solid lines) and $\tilde{h}^2$ (dashed lines) as functions of the wavenumber for experiment F4 (upper graph) and experiment F7 (lower graph).

although forcing and friction prevent it from being realized, the inviscid solution (6) remains a useful reference to analyse the steady flow and understand its correlation with the topographic field. Bretherton and Haidvogel (1976) and Herring (1977) reached similar conclusions based on their respective models.

The energy budget is represented in Figure 4. The mean forcing term does not appear since it is negligible compared with the energy input by wind fluctuations. As pointed out in Section 3, steady currents are forced by nonlinear interactions, and draw their energy from the mesoscale fluctuations. The topography does not appear in domain-averaged statistics. If the transfer terms were plotted as a function of wavenumber, the topography would appear as a transfer from large horizontal scales to smaller scales (Treguier and Hua, 1988).

4.2 Dependence on the Energy Level

In order to demonstrate the existence of the linear and nonlinear regimes

Table 2 Influence of the energy level in f-plane experiments. Units are $10^{-4}\,m^2\,s^{-2}$ for the rms zonal stress τ_0 and $10^{-7}\,s^{-1}$ for the bottom friction coefficient ε

Run	*Parameters (when different from Table 1)*	*Total rms u (cm/s)*	*Steady kinetic energy*	*$\langle \zeta h \rangle$ correlation*
F1	$\tau_0 = 1$	2	12%	0.5
F2	$\tau_0 = 2.5$	4	33%	0.6
F3	$\tau_0 = 5$	9	52%	0.8
F4	$\tau_0 = 7.5$	13	56%	0.9
F5	$\tau_0 = 10$	17	57%	0.9
F6	$\tau_0 = 15$	27	47%	1.0
F7	$\tau_0 = 20$	35	36%	1.0
F8	curl, $\tau_0 = 1$	3	27%	0.6
F9	curl, $\tau_0 = 2.5$	8	38%	0.7
F10	curl, $\tau_0 = 5$	15	38%	0.9
F11	curl, $\tau_0 = 7.5$	23	36%	0.9
F12	curl, $\tau_0 = 10$	31	34%	1.0
F13	curl, $\tau_0 = 15$	45	27%	1.0
F14	$\tau_0 = 10$, $\varepsilon = 4$	9	19%	0.7
F15	$\tau_0 = 10$, $\varepsilon = 2$	13	39%	0.9
F16	$\tau_0 = 10$, $\varepsilon = 0.5$	24	60%	1.0
F17	$\tau_0 = 10$, $\varepsilon = 0.25$	36	40%	1.0

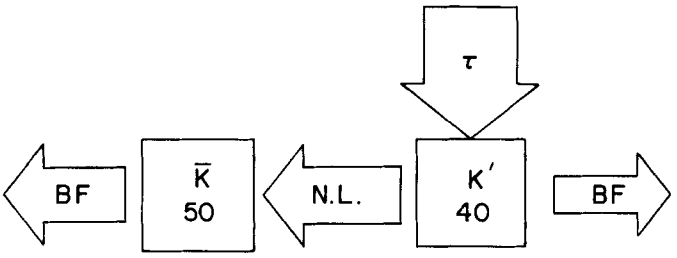

Figure 4 Energy budget for experiment F4. τ is the wind forcing, BF bottom friction, and NL nonlinear transfers. The thickness of the arrows is proportional to the strength of the energy transfers. The numbers in the boxes are the kinetic energies in $cm^2\,s^{-2}$.

suggested in Section 2, various experiments have been performed with increasing forcing (Table 2). Curve 1 of Figure 5 clearly demonstrates the non-monotonic dependence of the percentage of steady energy as a function of the total rms velocity u. The percentage of steady energy grows in the linear regime (at low energies) because the nonlinear transfer term in the energy budget grows more rapidly than the forcing term. On the other hand, the relative importance of steady currents decreases in the nonlinear regime (at high energies) since the nonlinear transfer term grows at a slower rate than the forcing term, because the flow is less constrained by the topography. Note that the steady currents always grow in

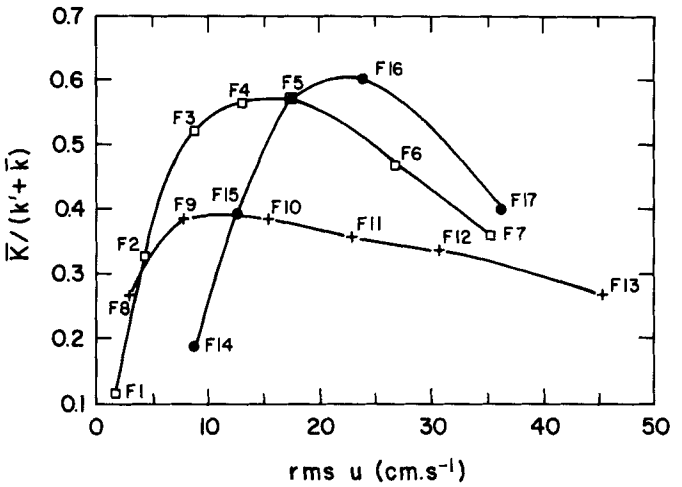

Figure 5 Percentage of steady kinetic energy as a function of the total rms velocity u for experiments of Table 2. Curve 1 (open squares): experiments F1 to F7 with a stress forcing. Curve 2 (crosses): experiments F8 to F13 with a curl forcing. Curve 3 (black dots): experiments F14 to F17 with variable bottom friction.

absolute value as the forcing energy increases, only their relative importance compared with the eddy currents decreases.

The position of the maximum depends on the forcing and dissipation mechanisms, as shown by curve 2 of Figure 5 (drawn for simulations forced by a large scale curl instead of a uniform stress) and curve 3 (simulations where the forcing is constant and the bottom friction coefficient varies). In the quasi-linear regime, simulations with a stronger dissipation have less steady energy for a similar energy level (curve 3 is below curve 1). The percentage of steady currents in our weakly nonlinear simulations is not simply proportional to the ratio of nondimensional forcing and friction $\hat{\tau}/\hat{\varepsilon}$ as suggested by the analytical calculation of Samelson and Allen (1987). This is not surprising since this particular result of their model depends crucially on the *a priori* assumption that the forcing and dissipation parameters are of the same order of magnitude, whereas the ratio of forcing and dissipation varies widely in our experiments.

4.3 Dependence on the Topography

The effect of the topographic rms height h cannot be studied independently from the effect of the energy level, since increasing the topographic height increases the dissipation. This happens because a higher topography enhances the cascade of energy toward small scales and therefore increases the amount of biharmonic friction. For example, the energy is 7 times smaller for simulation F31 with high topography ($h=800$ m) than for simulation F18 with low topography ($h=50$ m) although the forcing strength is the same (Table 3). In simulation F18, the energy

Table 3 Influence of the topography in f-plane experiments. Units are $10^{-4}\,m^2\,s^{-2}$ for the rms zonal stress τ_0 and 10^{-3} for the rms bottom slope α

Run	*Parameters (when different from Table 1)*	*total rms u (cm/s)*	*Steady kinetic energy*	$\langle \zeta h \rangle$ *correlation*
F18	$\tau_0 = 2.5, \delta = 0.01, \alpha = 0.8$	5	32%	0.8
F19	$\tau_0 = 7.5, \delta = 0.01, \alpha = 0.8$	13	37%	1.0
F20	$\tau_0 = 15, \delta = 0.01, \alpha = 0.8$	26	19%	1.0
F21	$\tau_0 = 2.5, \delta = 0.04, \alpha = 2.8$	4	25%	0.5
F22	$\tau_0 = 7.5, \delta = 0.04, \alpha = 2.8$	12	61%	0.8
F23	$\tau_0 = 15, \delta = 0.04, \alpha = 2.8$	25	66%	0.9
F24	$\tau_0 = 20, \delta = 0.04, \alpha = 2.8$	34	63%	0.9
F25	$\tau_0 = 2.5, \delta = 0.08, \alpha = 5.6$	3	14%	0.4
F26	$\tau_0 = 7.5, \delta = 0.08, \alpha = 5.6$	9	55%	0.6
F27	$\tau_0 = 10, \delta = 0.08, \alpha = 5.6$	13	63%	0.6
F28	$\tau_0 = 15, \delta = 0.08, \alpha = 5.6$	20	71%	0.7
F29	$\tau_0 = 18.5, \delta = 0.08, \alpha = 5.6$	25	72%	0.8
F30	$\tau_0 = 25, \delta = 0.08, \alpha = 5.6$	35	72%	0.8
F31	$\tau_0 = 2.5, \delta = 0.16, \alpha = 11.1$	2	5%	0.3
F32	$\tau_0 = 15, \delta = 0.16, \alpha = 11.1$	14	61%	0.5
F48	$\tau_0 = 20, \delta = 0.16, \alpha = 11.1$	20	67%	0.6
F49	$\tau_0 = 25, \delta = 0.16, \alpha = 11.1$	26	71%	0.7
F33	$\tau_0 = 30, \delta = 0.16, \alpha = 11.1$	32	73%	0.7
F34	$\tau_0 = 2.5, \alpha = 0.8, B(K) = K^{-3}$	4	27%	0.6
F36	$\tau_0 = 2.5, \alpha = 4.9, B(K) = (14)$	4	35%	0.9
F37	$\tau_0 = 7.5, \alpha = 0.8, B(K) = K^{-3}$	13	56%	0.9
F38	$\tau_0 = 7.5, \alpha = 4.9, B(K) = (14)$	13	22%	1.0
F39	$\tau_0 = 5, \delta = 0.16, \alpha = 11.1$	4	18%	0.4
F40	$\tau_0 = 10, \delta = 0.16, \alpha = 11.1$	8	44%	0.5
F41	$\tau_0 = 2.5, \alpha = 3.7, B(K) = (14)$	4	42%	0.9
F42	$\tau_0 = 5.0, \alpha = 0.8, B(K) = K^{-3}$	9	48%	0.8
F43	$\tau_0 = 5.0, \alpha = 4.9, B(K) = (14)$	8	32%	1.0
F44	$\tau_0 = 7.5, \alpha = 4.1, B(K) = (14)$	13	28%	1.0
F45	$\tau_0 = 15, \alpha = 0.8, B(K) = K^{-3}$	13	56%	0.9
F46	$\tau_0 = 15, \alpha = 4.1, B(K) = (14)$	26	11%	1.0
F47	$\tau_0 = 15, \alpha = 4.9, B(K) = (14)$	26	8%	1.0

is mainly dissipated by bottom friction and lateral friction represents only 2% of the total energy dissipation, whereas it represents 50% in experiment F31. This large influence of the topography on the energy level did not appear in Treguier and Hua (1988) probably because those simulations were baroclinic and the topographic spectrum was truncated at a wavelength of 130 km instead of 64 km in the present case.

Figure 6 shows the percentage of steady energy for various simulations in a (u, δ) plane (u being the rms velocity and $\delta = h/H$ the nondimensional topographic height). Increasing δ increases the maximum percentage of steady currents. For the experiments with $\delta = 0.01$ the percentage of steady kinetic energy remains below 40% whereas it reaches a maximum of about 72% with $\delta = 0.08$. Increasing δ also shifts the position of the maximum to the right (to larger u). This is consistent

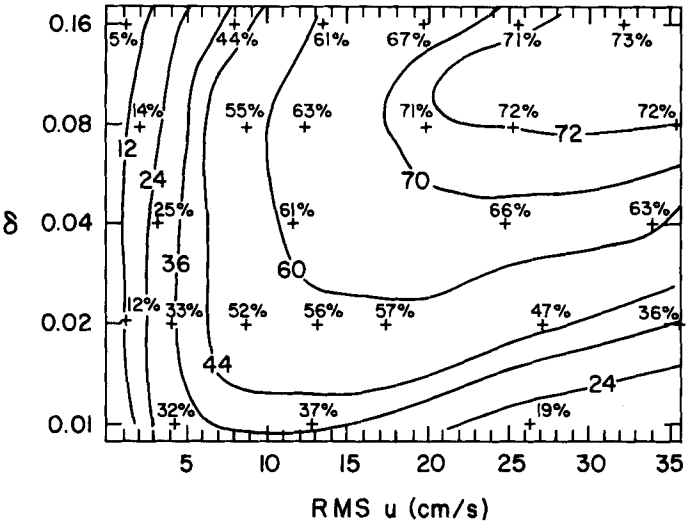

Figure 6 Percentage of steady kinetic energy in a $(u, \log \delta)$ plane for experiments F1 to F7 (Table 2) and experiments F18 to F38 (Table 3). Contours are drawn subjectively.

with a dependence on the ratio R_0/δ, R_0 being the Rossby number u/fL. When h grows at a fixed energy level (along a vertical line in Figure 6), the percentage of steady currents first increases as found by Herring (1977) and Holloway (1978). A new result of our simulations is the decrease for high topographies. In that limit, the flow tends toward a quasi-linear regime where nonlinear terms become less important compared to forcing and dissipation.

Simulations have also been performed with different topographic spectra. One may expect a decrease in the topographic horizontal scale to have the same effect as an increase of δ, since it is the topographic slope α rather than the topographic height which emerges from a scaling of the vorticity equation. This appears to be true qualitatively, but not quantitatively. Figure 7 shows the steady energy as a function of the rms topographic slope α for simulations with different energy levels. The percentage of steady currents grows first, and then decreases as the topographic horizontal scale $\bar{K}_t^{-1}$ becomes smaller. The maximum of the curves shifts towards smaller values of α when forcing increases. For large $\bar{K}_t$ steady currents decrease because the flow becomes relatively more linear, as happened for large δ. However, the dynamics of the large δ simulations are quite different from those of the large $\bar{K}_t$ simulations. With a large δ, the fluctuating field contains energetic topographic Rossby waves, and the eddy vorticity is large. With a large $\bar{K}_t$, the fluctuating field consists mainly of a large scale flow U' directly forced by the wind, and the eddy vorticity is small. The generation of eddy vorticity from the large scale flow is not efficient when the topographic horizontal scale $\bar{K}_t^{-1}$ is small compared with the length scale $U'\theta$ (θ being a typical time scale). Since U' represents most of the eddy energy when $\bar{K}_t$ increases, there is no decrease of the global energy level due to enhanced small scale dissipation, contrary to the case of increasing δ.

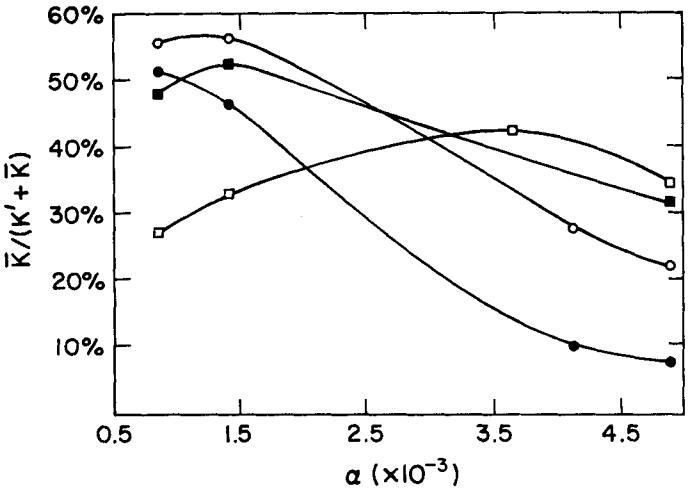

Figure 7 Percentage of steady kinetic energy as a function of the rms slope α for the experiments of Table 3 where the topographic spectrum ($\delta = 0.02$ is fixed). Open squares: experiments with $\tau = 2.5 \times 10^{-4}$. Open circles: experiments with $\tau = 5 \times 10^{-4}$. Black squares: experiments with $\tau = 7.5 \times 10^{-4}$. Black circles: experiments with $\tau = 15 \times 10^{-4}$.

Because of those different dynamics, the effect of topography on steady currents cannot be represented by the single parameter α. For example, simulations F27 and F38 in Table 3 have identical energy levels and similar values of α, but the percentages of steady currents are very different (63% and 22% respectively) because δ and $\bar{K}_t$ vary.

5. SIMULATIONS IN A β-PLANE CHANNEL

5.1 Dynamics

The presence of the β effect does not affect much the eddy space and time scales, nor the eddy energy level. The global shape of the frequency spectra is the same as in the f-plane case, although resonant peaks corresponding to the largest scale (smallest frequency) barotropic Rossby waves are present when β is non zero.

The steady flow, on the contrary, is completely modified by the β effect. First, the amount of steady energy is lower than in the f-plane case. Since it is not due to a smaller reservoir of eddy energy, the decrease of the nonlinear transfer term can be understood only in terms of modified correlations, due to the phase propagation induced by β. Secondly, the large scale steady flow $\bar{U}$ is much larger. For simulation B3 in Table 4, $\frac{1}{2}\bar{U}^2$ represents two thirds of the total steady kinetic energy (*vs* less than 1% for simulation F4 with $\beta = 0$). The time-averaged transport is 411 Sv, and $\bar{U} = 6$ cm/s.

The importance of $\bar{U}$ is obvious in the steady streamfunction maps (Figure 8). As in the f-plane case, it is useful to compare the solution with the theoretical form (6). Now two relationships have to be tested. In the inviscid solution, the x-

Table 4 Influence of the energy level in β-plane experiments. Units are $10^{-4}\,m^2\,s^{-2}$ for the rms zonal stress τ_0 and $10^{-11}\,m^{-1}\,s^{-1}$ for β. u is the total rms velocity (cm/s), $\bar{u}$ the rms velocity associated with the "mesoscale" steady flow $\bar{\psi}$ (cm/s) and $\bar{U}$ the steady uniform westward flow (cm/s)

Run	*Parameters (when different from Table 1)*	u	$\bar{u}$	$\bar{U}$	*Steady kinetic energy*	$\langle\zeta h\rangle$ *correlation*
B1	$\tau_0 = 2.5, \beta = 1.5$	4	2	1	29%	0.6
B2	$\tau_0 = 5, \beta = 1.5$	9	4	4	36%	0.7
B3	$\tau_0 = 7.5, \beta = 1.5$	13	5	6	38%	0.7
B4	$\tau_0 = 10, \beta = 1.5$	18	6	9	38%	0.8
B5	$\tau_0 = 15, \beta = 1.5$	27	9	14	39%	0.8
B6	$\tau_0 = 20, \beta = 1.5$	36	11	20	39%	0.8
B7	$\tau_0 = 30, \beta = 1.5$	53	15	29	37%	0.8
B8	curl, $\tau_0 = 1, \beta = 1.5$	8	3	3	32%	0.6
B9	curl, $\tau_0 = 2.5, \beta = 1.5$	15	7	6	35%	0.7
B10	curl, $\tau_0 = 5, \beta = 1.5$	22	10	9	36%	0.8
B11	curl, $\tau_0 = 7.5, \beta = 1.5$	43	17	19	35%	0.8

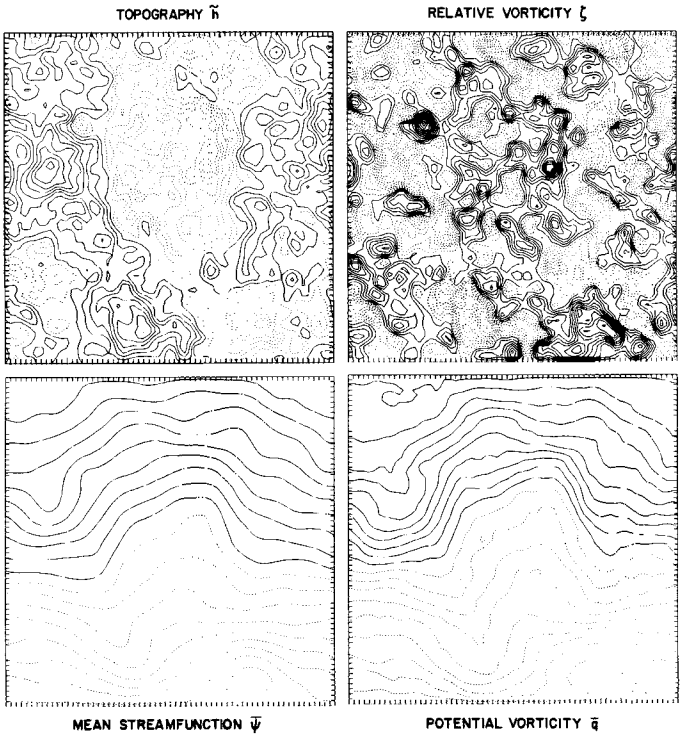

Figure 8 Time-averaged fields for experiment B3. Contour intervals are 40 m for the topography, $3\times10^{-7}\,s^{-1}$ for the relative vorticity $\bar{\zeta}$, $5000\,m^2\,s^{-1}$ for the streamfunction $\bar{\psi}$, and $10^{-6}\,s^{-1}$ for the potential vorticity $\bar{q}=\bar{\zeta}+\tilde{h}$.

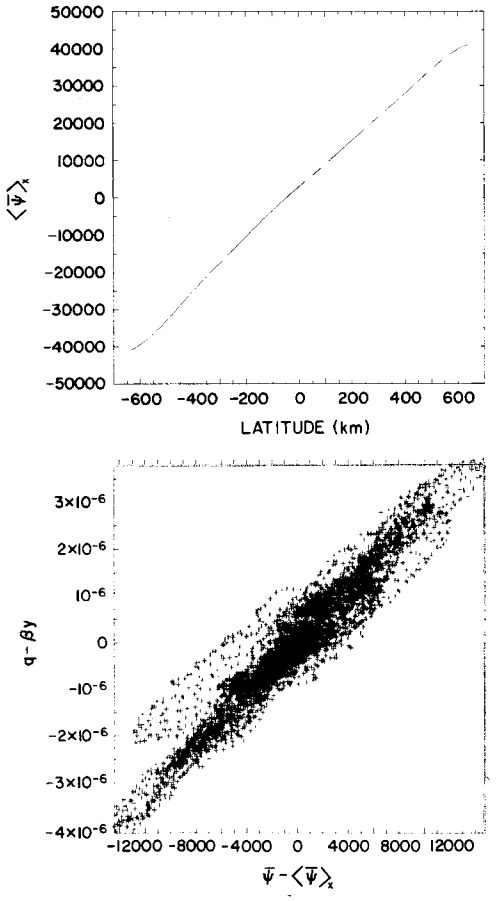

Figure 9 (a) Zonally averaged total streamfunction $\langle\bar{\Psi}\rangle_x$ as a function of latitude for experiment B3; (b) Potential vorticity $\bar{q}-\beta y$ as a function of $\bar{\Psi}-\langle\bar{\Psi}\rangle_x$ for all grid points for the same experiment.

averaged "mesoscale" streamfunction vanishes ($\langle\bar{\psi}\rangle_x=0$) and therefore the total streamfunction satisfies $\langle\bar{\Psi}\rangle_x=-\bar{U}y$. In simulation B3, this relation is only approximately satisfied as appears in Figure 9a, which shows $\langle\bar{\Psi}\rangle_x$ as a function of latitude. The departure from a linear relationship is greater near the boundaries. However, the agreement is much better in most of our simulations than it was in Bretherton and Haidvogel's (1976) free turbulence experiments (see their Figure 11). Because $\langle\bar{\Psi}\rangle_x$ is not a linear function of y, $(\bar{\Psi}-\bar{U}y)$ contains a linear trend and does not satisfy (6). However, $\bar{\Psi}-\langle\bar{\Psi}\rangle_x$ tends to be linearly related with $\bar{\zeta}+h$ as shown in Figure 9b. The larger scatter than in Figure 2b, as well as the fact that the correlation coefficient between the relative vorticity and the topography drops from 0.9 in simulation F4 to 0.7 in simulation B3, both confirm that the departure from the theoretical solution is larger when β is non zero. This was expected, since without that departure the time-averaged topographic drag would vanish and $\bar{U}$ would be zero according to the energy equation (9). Nonetheless, the

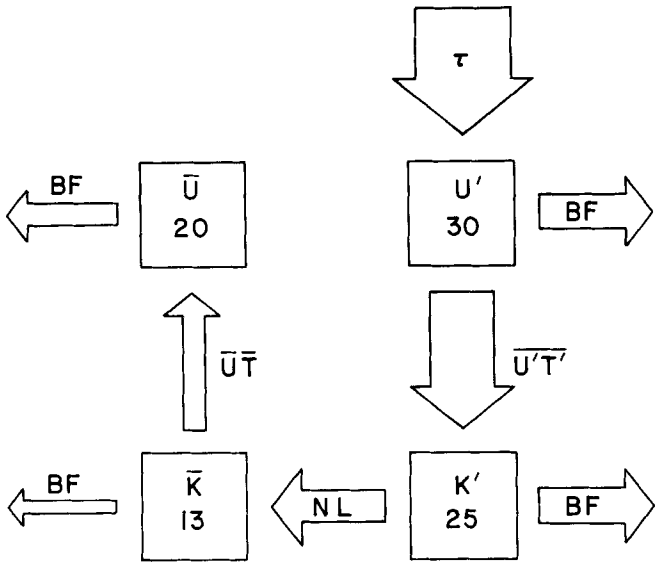

Figure 10 Energy budget for experiment B3. The thickness of the arrows is proportional to the strength of the energy transfers. The numbers in the boxes are the kinetic energies in $cm^2 s^{-1}$.

theoretical solution (6) is still a useful reference in analysing steady currents in β-plane topographic turbulence.

In the energy budget (Figure 10) the zonal flow U and the "mesoscale" ψ have been separated, in order to show better the two-step process leading to the generation of $\bar{U}$. In this special case of a uniform zonal stress, only the U' component is directly forced by the wind and ψ would remain zero in the absence of topography. Mesoscale fluctuations ψ' ar forced by a term which could be called the "eddy topographic drag" $\overline{U'T'}$ with

$$U'T' = A^{-1}U' \int\int v'\tilde{h}\,dx\,dy.$$

As in the f-plane case, the steady mesoscale flow $\bar{\psi}$ is forced by nonlinear interactions. Then, in a second step, energy is transferred from $\bar{\psi}$ to the mean zonal flow $\bar{U}$ through the topographic drag term $\bar{U}\bar{T}$. The energy equilibrium for $\bar{U}$ is simply (9) since the steady forcing is one order of magnitude smaller than the other terms. Evaluating the terms in (10), we find that for this simulation mesoscale and large scale steady currents are of the same order of magnitude ($\bar{U}/\bar{u} \approx 1$), and the correlation C between $\bar{v}$ and h is small ($C \approx \varepsilon/\tilde{h} \approx 0.05$). C measures how a solution departs from the inviscid solution (6), since C is zero in the inviscid case. It will be shown in the following sections that C is small unless β becomes large compared to the mesoscale rms topographic slope.

Table 5 Influence of the topography in β-plane experiments. Units are $10^{-11}\,m^{-1}\,s^{-1}$ for β, $10^{-4}\,m^2\,s^{-2}$ for τ_0, and 10^{-3} for the topographic slope α. u is the total rms velocity (cm/s), $\bar{u}$ the rms velocity associated with the "mesoscale" steady flow $\bar{\psi}$ (cm/s), and $\bar{U}$ the steady uniform westward flow (cm/s)

Run	*Parameters (when different from Table 1)*	u	$\bar{u}$	$\bar{U}$	*Steady kinetic energy*	$\langle \zeta h \rangle$ *correlation*
B12	$\tau_0 = 2.5, \beta = 0.5$	4	2	1	32%	0.6
B13	$\tau_0 = 2.5, \beta = 2$	4	2	2	27%	0.6
B14	$\tau_0 = 2.5, \beta = 5$	4	1	2	19%	0.4
B15	$\tau_0 = 2.5, \beta = 20$	4	0.3	1	6%	0.1
B16	$\tau_0 = 15, \beta = 0.5$	27	14	12	48%	0.9
B17	$\tau_0 = 15, \beta = 2$	26	7	14	36%	0.7
B18	$\tau_0 = 15, \beta = 5$	26	5	13	26%	0.5
B19	$\tau_0 = 15, \beta = 20$	26	2	8	10%	0.3
B20	$\tau_0 = 2.5, \beta = 20, \delta = 0.005, \alpha = 0.3$	4	0.1	1	2%	0.03
B21	$\tau_0 = 2.5, \beta = 5, \delta = 0.01, \alpha = 0.7$	4	0.5	1	9%	0.3
B22	$\tau_0 = 15, \beta = 5, \delta = 0.01, \alpha = 0.7$	26	3	8	11%	0.4
B23	$\tau_0 = 2.5, \beta = 1.5, \delta = 0.01, \alpha = 0.7$	4	1	0.6	19%	0.5
B24	$\tau_0 = 2.5, \beta = 1.5, \delta = 0.04, \alpha = 2.8$	4	2	0.6	26%	0.5
B25	$\tau_0 = 2.5, \beta = 1.5, \delta = 0.08, \alpha = 5.6$	3	1	0.2	14%	0.4
B26	$\tau_0 = 15, \beta = 1.5, \delta = 0.16, \alpha = 11.1$	2	0.4	0.04	5%	0.3
B27	$\tau_0 = 15, \beta = 1.5, \delta = 0.01, \alpha = 0.7$	27	6	11	23%	0.7
B28	$\tau_0 = 15, \beta = 1.5, \delta = 0.04, \alpha = 2.8$	25	14	11	53%	0.8
B29	$\tau_0 = 15, \beta = 1.5, \delta = 0.08, \alpha = 5.6$	20	15	5	65%	0.7
B30	$\tau_0 = 15, \beta = 1.5, \delta = 0.16, \alpha = 11.1$	14	10	2	58%	0.5
B31	$\tau_0 = 2.5, \beta = 1.5, B(K) = K^{-3}, \alpha = 0.8$	4	1	1	19%	0.5
B32	$\tau_0 = 2.5, \beta = 1.5, B(K) = (14), \alpha = 4.9$	4	2	1	35%	0.9
B33	$\tau_0 = 7.5, \beta = 1.5, B(K) = K^{-3}, \alpha = 0.8$	13	4	6	30%	0.6
B34	$\tau_0 = 7.5, \beta = 1.5, B(K) = (14), \alpha = 4.9$	13	5	6	33%	1.0
B35	$\tau_0 = 15, \beta = 1.5, B(K) = K^{-3}, \alpha = 0.8$	26	8	13	36%	0.7
B36	$\tau_0 = 15, \beta = 1.5, B(K) = (14), \alpha = 4.9$	26	6	9	18%	1.0

5.2 Dependence on the Energy Level

The steady zonal flow $\bar{U}$ grows as the energy level grows (Table 4), as was found by Holloway (1987) and Haidvogel and Brink (1987). Haidvogel and Brink also noted an increase in steady currents when the frequency of the forcing was decreased, which was at least partly due to the increased energy of the response for low frequency forcing. The growth of both the mesoscale and the large scale steady energy becomes slightly slower at the highest energy levels and therefore the percentage of steady energy begins to decrease (Table 3) as in the f-plane case, but the decrease happens at larger energies.

5.3 Effects of β and α

Increasing the topographic height δ or the rms topographic slope α decreases the energy level by enhancing biharmonic friction as happened in the f-plane case (Table 5). The effect of topography on steady currents is stherefore not easy to

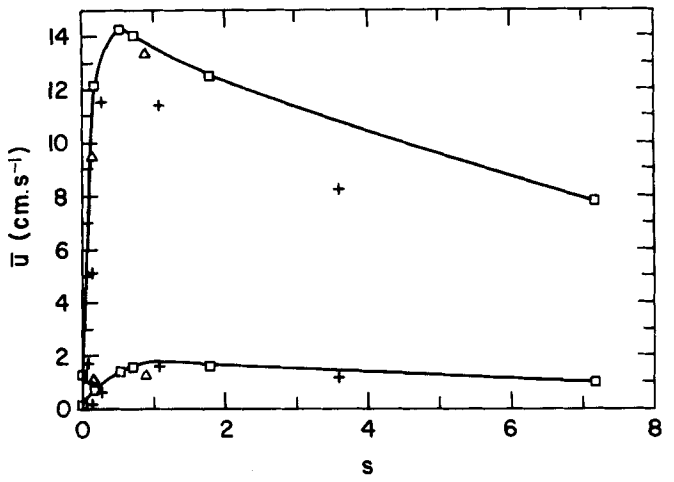

Figure 11 Steady westward flow $\bar{U}$ as a function of $S=\beta H/f_0\alpha$. The lower curve is for experiment in Tables 4 and 5 with $\tau_0=2.5$ and the upper curve for $\tau_0=15$. The squares along the curves are for experiments in which β varies. Crosses are for experiments in which δ varies, and triangles for experiments in which the topographic spectrum varies.

study independently. Fortunately, the effect of β and h on the westward flow $\bar{U}$ can be understood in terms of a single parameter, $S=\beta H/f_0\alpha$. S is the ratio of the "large scale" bottom slope equivalent to the β-effect, $\beta H/f_0$, and the "mesoscale" bottom slope α. The importance of this parameter was noted in the weakly nonlinear case by Samelson and Allen (1987). and is confirmed in the nonlinear case by our simulations.

Figure 11 represents $\bar{U}$ as a function of S for low energy simulations with different β (lower curve) and high energy simulations with different β (upper curve). The dependence is non-monotonic. For $S\ll 1$, there may be a large reservoir of mesoscale steady energy, but the steady streamfunction is well correlated with the topography, $\bar{\psi}$ is close to the inviscid solution (6), and therefore the time averaged topographic drag $\bar{T}$ is very small. The westward flow $\bar{U}$ is small in the limit of small S. On the other hand, when S is large, the phase propagation induced by β prevents the efficient generation of mesoscale steady currents. Since $\bar{u}$ is small, the topographic drag $\bar{T}$ is also small, and $\bar{U}$ decreases in the limit of large S. This decrease was observed by Haidvogel and Brink (1986), since S was much larger than one in all their simulations. The maximum westward flow in Figure 11 occurs for $S\approx 1$ and is closer to $S=1$ in the low energy limit as in Samelson and Allen (1987). When $S\approx 1$, mesoscale and large scale steady currents are of the same order of magnitude almost whatever the energy level (Figure 12). Since the westward steady flow $\bar{U}$ draws its energy from the mesoscale steady flow this situation is the most favorable for an efficient westward flow generation; hence, the maximum of $\bar{U}$ for $S\approx 1$. Note that a plot of the steady topographic drag $\bar{T}$ as a function of S would be identical in shape, since from (9)

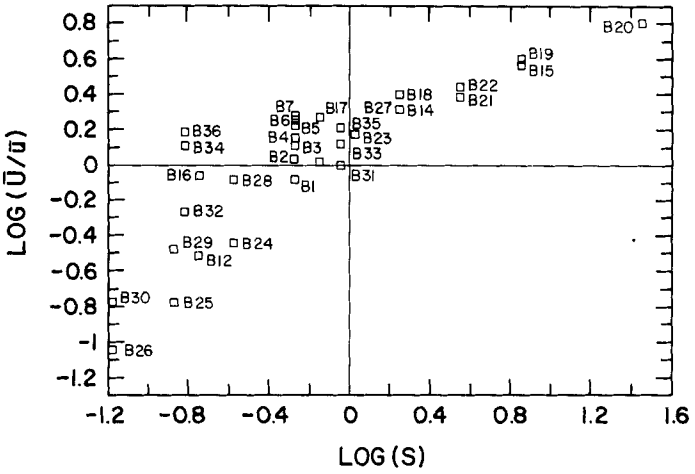

Figure 12 Ratio $\bar{U}/\bar{u}$ of large scale to mesoscale steady currents as a function of S in a logarithmic scale, for all experiments of Table 4 and Table 5.

$\bar{T}=\varepsilon\bar{U}$, and the bottom friction coefficient ε is the same for all simulations in Figure 11.

Of course, the variations of $\bar{U}$ from one simulation to the other cannot be all related to changes in S. Experiments with different values of δ and β do not fit on the same curve in Figure 11, because changing β does not affect the energy level whereas changing δ does. We also find, as for the f-plane case, that variations of topographic height h do not have exactly the same effect as variations of the topographic horizontal scale, and therefore the effect of the topography is not completely described by the parameter α alone. Even with those limitations, S appears as the most useful parameter to characterize *qualitatively* the behavior of the steady westward flow.

Figure 12 shows that the ratio of large scale and mesoscale steady currents $\bar{U}/\bar{u}$ is an increasing function of S, with a smaller dependence on other parameters (different energy level is the main source of scatter). $\bar{U}/\bar{u}$ does not grow when h grows as the scaling (10) of the energy equation suggests but rather decreases, because the better correlation of the mesoscale steady currents with the topography makes the topographic drag smaller. From (10), $\bar{U}/\bar{u}$ would appear to depend strongly on the bottom friction coefficient. This is not the case in our experiments because a decrease in ε allows the flow to be closer to the inviscid solution (6), and a decrease of the topographic drag $\bar{T}$ compensates the decrease of ε. The same compensation occurs in Samelson and Allen's (1987) weakly nonlinear solution. Their first order steady streamfunction is perfectly correlated with the topography and the time-averaged topographic drag $\bar{T}$ vanishes at leading order, because the bottom friction parameter appears only at second order.

6. CONCLUSION

The generation of steady currents in barotropic topographic turbulence has been analysed. The relationship between mesoscale steady currents following mesoscale topographic features, and the large scale zonal flow due to the β effect, is clear when energy budgets are considered. When there is no steady forcing, mesoscale steady currents can be maintained against dissipation by drawing energy from mesoscale fluctuations, through nonlinear interactions. The large scale zonal flow is forced by the topographic drag acting on the mesoscale steady circulation, and thus draws its energy from it.

Because of forcing and dissipation, the steady flow in our experiments differs from the inviscid statistical equilibrium solution, especially when β is non zero. However, the steady flows still exhibit the qualitative features of the theoretical inviscid solution: the correlation of streamfunction and topography at large scales, the anticorrelation of relative vorticity and topography at small scales, and the linear shape of the zonally averaged steady streamfunction when β is non zero.

The present set of simulations provides a comprehensive picture of the behavior of steady currents in parameter space. In the quasi-linear regime studied by Samelson and Allen (1987), the percentage of steady currents grows with the energy level, while it decreases in the nonlinear regime studied by Herring (1977) and Holloway (1978). Our simulations show the continuity between those two regimes, and show that the dependence on the rms topographic height or slope is similarly non-monotonic. In the β-plane case the westward flow $\bar{U}$ depends essentially on the parameters $S=\beta H/f_0\alpha$ which is the ratio of the large scale slope $\beta H/f_0$ and the mesoscale slope α. $\bar{U}$ is maximum for $S\approx 1$. In that case the large scale and mesoscale steady flows are of the same order of magnitude, and since they are coupled it is the situation most favorable for steady flow generation.

These barotropic simulations have been performed to clarify the dynamics of steady currents in the simplest case possible. The results will help design baroclinic experiments, which will provide more quantitative results and allow the examination of the vertical structure of steady currents.

Acknowledgements

This work was stimulated by helpful discussions with Jim McWilliams and Jack Herring. I thank also D. Haidvogel and G. Holloway for their comments on an early version of the manuscript. The National Center for Atmospheric Research is sponsored by the National Science Foundation.

References

Bretherton, F. P. and Karweit, M. J. "Mid-ocean mesoscale modelling," in: *Numerical Models of Ocean Circulation*, Ocean Affairs Board of the National Research Council, 237 (1975).

Bretherton, F. P. and Haidvogel, D. B., "Two dimensional turbulence above topography," *J. Fluid Mech.* **78**, 129 (1976).

Carnevale, G. F. and Frederiksen, J. S., "Nonlinear stability and statistical mechanics of flow over topography," *J. Fluid Mech.* **175**, 157 (1987).

Haidvogel, D. B. and Brink, K. H., "Mean currents driven by topographic drag over the continental shelf and slope," *J. Phys. Oceanogr.* **16,** 2159 (1986).

Herring, J. R., "On the statistical theory of two dimensional topographic turbulence," *J. Atmos. Sci.* **34,** 1731 (1977).

Holloway, G., "A spectral theory of non linear barotropic motion above irregular topography," *J. Phys. Oceanogr.* **8,** 414 (1978).

Holloway, G., "Systematic forcing of large-scale geophysical flows by eddy–topography interaction," *J. Fluid Mech.* **184,** 463 (1987).

McWilliams, J. C., "A note on a consistent quasi-geostrophic model in a multiply connected domain," *Dyn. Atmos. Oceans* **1,** 427 (1977).

McWilliams, J. C. and Chow, J., "Equilibrium turbulence I: a reference solution in a β-plane channel," *J. Phys. Oceanogr.* **11,** 921 (1981).

Salmon, R., Holloway, G. and Henderschott, M. C., "The equilibrium statistical mechanics of simple quasi-geostrophic models," *J. Fluid Mech.* **75,** 691 (1976).

Samelson, R. M. and Allen, J. S., "Quasi-geostrophic topographically generated mean flow over the continental margin," *J. Phys. Oceanogr.* **17,** 2043 (1987).

Treguier, A. M. and Hua, B. L., "Oceanic quasi-geostrophic turbulence forced by stochastic wind fluctuations," *J. Phys. Oceanogr.* **17,** 397 (1987).

Treguier, A. M. and Hua, B. L., "Influence of bottom topography on quasi-geostrophic turbulence in the ocean," *Geophys. Astrophys. Fluid Dynam.*, **43,** 2 65–305 (1988).